UNIVERSITAT POLITÈCNICA DE VALÈNCIA

UNIVERSITAT POLITÈCNICA DE VALÈNCIA

CAMPUS DE GANDIA

UNIVERSITAT POLITÈCNICA DE VALÈNCIA

Higher Polytechnic School of Gandia

Bidirectional holograms for transcranial therapeutic ultrasound

Master's Thesis

Master's Degree in Acoustic Engineering

AUTHOR: Valle Sánchez, Marta

Tutor: Camarena Femenia, Francisco

External cotutor: Jiménez González, Noé

Experimental director: Eroles Simó, Alba

ACADEMIC YEAR: 2024/2025

Acknowledgements

A Gandía y a su gente, por darme uno de los años más bonitos de mi vida.

A mamá, papá y Carlos, por brindarme la oportunidad de salir y conocer.

A Cano, por todas las cosas que me enseñaste y aún laten aquí dentro.

Abstract

Acoustic holograms are emerging as a new therapeutic approach to focus ultrasound energy into human tissues. Holograms are suited to generate sharp acoustic images and, in addition, the phase aberrations produced by tissues such as skull bones can be compensated. However, these lenses present a rough and irregular shape that make difficult its coupling with the human skin. In this work, we exploit the reciprocity of the mechanical waves to manufacture lenses that present either a flatter surface in the radiating face. This face can be designed to fit over the skin, easily adapting to different anatomical areas of the head, such as the temporal bone window, enhancing the coupling of the lens to the patient head. To validate this approach a set of acoustic simulations considering different materials to design the holographic lens are considered. In this way, this approach results in a compact wearable device for transcranial therapeutic ultrasound applications such as neuromodulation, localized drug delivery or focused hyperthermia.

Keywords Acoustic holograms; Transcranial therapeutic ultrasound; Matching layers.

Resumen

Los hologramas acústicos están emergiendo como un nuevo enfoque terapéutico para focalizar energía ultrasónica en los tejidos humanos. Estas hologramas son idóneas para generar imágenes acústicas nítidas y, además, permiten compensar las aberraciones de fase producidas por tejidos como el hueso craneal. Sin embargo, estas lentes presentan una forma rugosa e irregular que dificulta su acoplamiento con la piel humana. En este trabajo, se explota la reciprocidad de las ondas mecánicas para fabricar lentes que presentan una superficie más plana en la cara emisora. Esta cara puede diseñarse para ajustarse sobre la piel, adaptándose fácilmente a distintas zonas anatómicas de la cabeza, como la ventana ósea temporal, mejorando así el acoplamiento de la lente con la cabeza del paciente Para validar este enfoque, se ha considerado un conjunto de simulaciones acústicas utilizando diferentes materiales para diseñar la lente holográfica. De esta manera, este método da lugar a un dispositivo compacto y portátil para aplicaciones terapéuticas de ultrasonido transcraneal, tales como neuromodulación, administración localizada de fármacos o hipertermia focalizada.

Palabras clave Hologramas acústicos; Terápias transcraneles con ultrasonido; Lentes anatómicas.

Contents

1 Introduction **8**

1.1 Motivation 8

1.2 Objectives 10

2 State of art **13**

2.1 Acoustic lenses and holography 13

2.2 Transcranial ultrasound therapy 15

3 Materials and methods **17**

3.1 Materials 17

3.1.1 Skull 18

3.1.2 Transducer 20

3.1.3 Lens and coupling material 20

3.2 Modeling of the acoustic field 22

3.3 Holographic lens design 24

3.3.1 Lens design 25

3.3.2 Generated acoustic fields 27

3.4 Study design 32

3.4.1 Study configuration 32

3.4.2 Metrics 34

4 Results **38**

4.1 Pressure distribution at the focal point 38

4.1.1 2D visualization of the acoustic pressure field 39

4.1.2 1D line profiles of the acoustic field 41

4.2 Quantitative analysis of the lens performance 45

4.2.1 Acoustic gain 45

4.2.2 Focal deviation 47

4.2.3 Depth of focus 48

4.2.4 Full Width at Half Maximum (FWHM) 50

5 Conclusions **53**

5.1 Future work 55

Chapter 1

Introduction

1.1 Motivation

The brain can be affected by various injuries and pathological conditions, including neurodegenerative disorders like Parkinson's and Alzheimer's disease, as well as neoplastic lesions such as tumors. These pathologies can be treated with different techniques including surgery, radiotherapy, or chemotherapy. Traditional techniques are invasive and often carry significant risks and potential side effects. As a result, emerging approaches are increasingly focused on non-invasive strategies that aim to improve both the precision and safety of therapies for neurological disorders. One of the emerging techniques currently under investigation is transcranial therapeutic ultrasound [1], [2]. This method is both non-ionizing and non-invasive, and it allows for the targeting of specific regions within the brain.

Several focal systems can be employed to achieve precise ultrasound energy delivery to specific brain regions. *Ultrasonic implants* are surgically inserted devices placed inside

the skull, thereby avoiding the acoustic distortions—such as refraction and reflection—caused by cranial bone [3], [4]. *Monoelement transducers*, composed of a single ultrasound emitter with a defined aperture, generate a focused beam at a specific point [5], [6]. *Magnetic Resonance-guided Focused Ultrasound* (MRgFUS) combines a phased array of ultrasound transducers with real-time MRI, enabling a continuous monitoring throughout the treatment [7], [8]. Lastly, *holographic lenses* are custom-designed devices placed in front of the transducer to manipulate the incident wavefront and compensate the skull-induced aberrations [9]–[11].

Just as optical holograms are capable of shaping light wavefronts to produce visible images [12], holographic acoustic fields—formed through controlled ultrasound propagation—offer a promising method to achieve similar spatial control in the acoustic domain. These fields are three-dimensional patterns engineered to control the propagation of ultrasound waves—including their phase and amplitude- usually, holograms are produced by passive lenses such as 3D-printed phase plates [9]–[11].

This approach enables the generation of complex wavefronts capable of precisely focusing acoustic energy on specific brain regions [11], [13]. Such precision is crucial due to the significant mismatch in acoustic properties between the skull and surrounding media, like water, which leads to phase aberrations that distort the ultrasound beam. By accurately compensating for these aberrations, it is possible to restore the integrity of the beam and achieve high spatial resolution at the focal zone, thereby enhancing the precision and efficacy of transcranial ultrasound treatments for neurological disorders.

Holographic fields can be generated using phased arrays, which are multielement transducers that can electronically vary the amplitude and phase of each element individually to generate tailored acoustic patterns [14]. However, this method is limited by the number and complexity of active radiating elements. The advent of advanced 3D printing

technologies has opened new possibilities, enabling the fabrication of custom-designed structures—such as complex phase plates [15]—capable of shaping acoustic wavefronts with high spatial resolution and flexibility. This allows for the treatment of neurological targets beyond the cortical surface, commonly referred to as deep brain structures.

These plates, known as holographic lenses, offer an alternative to phased arrays by enabling a single-element transducer to modulate its initially planar wavefront when placed in contact with the lens surface. Designed to be positioned directly over the transducer, these lenses can steer and focus ultrasound waves toward specific brain regions. However, precise alignment and coupling of the lens to the patient's head is critical to ensure that the acoustic energy is accurately directed and reaches the intended focal point. In prior work, the lens was designed to be immersed in a water tank allowing the propagation of the ultrasounds that come form the transducer and focus inside patient's head. However, this setup is impractical for use in real patients due to its complexity in clinical environments, where the hologram surface couples to an arbitrary anatomical surface like the skin of the patitent's head.

1.2 Objectives

Since ultrasound waves do not propagate through air, the lens must be in direct contact with a coupling medium to allow effective transmission through the lens and toward the target area. This contact is essential to ensure efficient energy transfer. However, achieving proper coupling can be complex due to the irregular shape of the human head anatomy, the surface roughness of the lens, and the need for precise alignment with the ultrasound transducer.

To address this challenge, the research presented in this work aims to develop a bi-

directional holographic lens that couples precisely to the user's physiognomy, thereby enhancing ultrasound wave propagation during transcranial therapies. Two distinct materials are defined on either side of the holographic plane: one representing the lens and the other the coupling medium, as illustrated in Figure 1.1. The analysis focuses on evaluating various material combinations along the ultrasound transmission path. Specifically, three configurations are investigated: low acoustic impedance with water, high acoustic impedance with water, and a combination of low and high acoustic impedance materials.

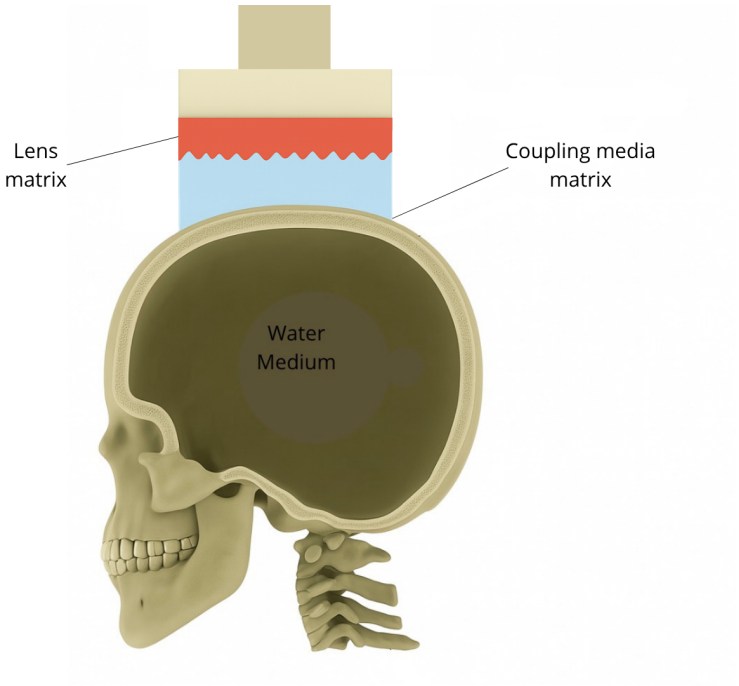


Figure 1.1: Schematic representation of the mediums distribution in the experimental setup.

Based on pseudospectral simulations, several key parameters will be evaluated to characterize the performance of the different material combinations used in the lens design. These parameters include the maximum pressure at the focal point, the deviation from the intended target, the focal length, and the beam width. To account for inter-subject variability, the tests will be conducted using three different ex-vivo skulls. This approach

not only allows for a comparative analysis of the material pairings but also enables the evaluation of patient-specific uncertainty, providing a more robust assessment of the lens's focusing performance across varying cranial anatomies.

Chapter 2

State of art

2.1 Acoustic lenses and holography

Holographic acoustic fields are often synthesized using phased arrays—assemblies of multielement transducers [16] that can be electronically controlled to modulate each element phase and amplitude in order to generate intricate wave patterns [17]–[19]. However, the number of active radiating elements in such arrays is typically limited up to one thousand, which constrains the achievable complexity and resolution of the resulting holographic fields. Besides this limitation, the cost of these devices is high, and they are not easily accessible for many applications.

In recent years, the advent of 3D printing technology has facilitated the creation of passive lenses and structures that can manipulate wavefronts reducing the cost and the drawbacks of traditional phased arrays. One such structure is the holographic phase plate [9], which is specifically designed to modulate the propagation of ultrasound waves. These lenses enable the formation of single focal points [10], customized therapeutic patterns

[20], [21], and vortex beams [20], [22], offering the ability to compensate for skull-induced aberrations [23] in transcranial ultrasound therapies.

Holographic lenses are designed to precisely control both the amplitude and phase of an incident acoustic wavefront. The fundamental principle is based on prescribing the desired acoustic field at a particular location—typically a focal point—on a designated plane known as the holographic plane. Using this target field, a time-reversal simulation is performed to compute the complex conjugate of the wavefront that would have been emitted from the focal point. The resulting distribution is then encoded into the lens structure [24]. When a planar wave emitted by a single-element transducer propagates through this lens, the conjugated wavefront is reconstructed, causing the ultrasound energy to converge at the desired target. This process, known as holographic focusing, is conceptually illustrated in Figure 2.1.

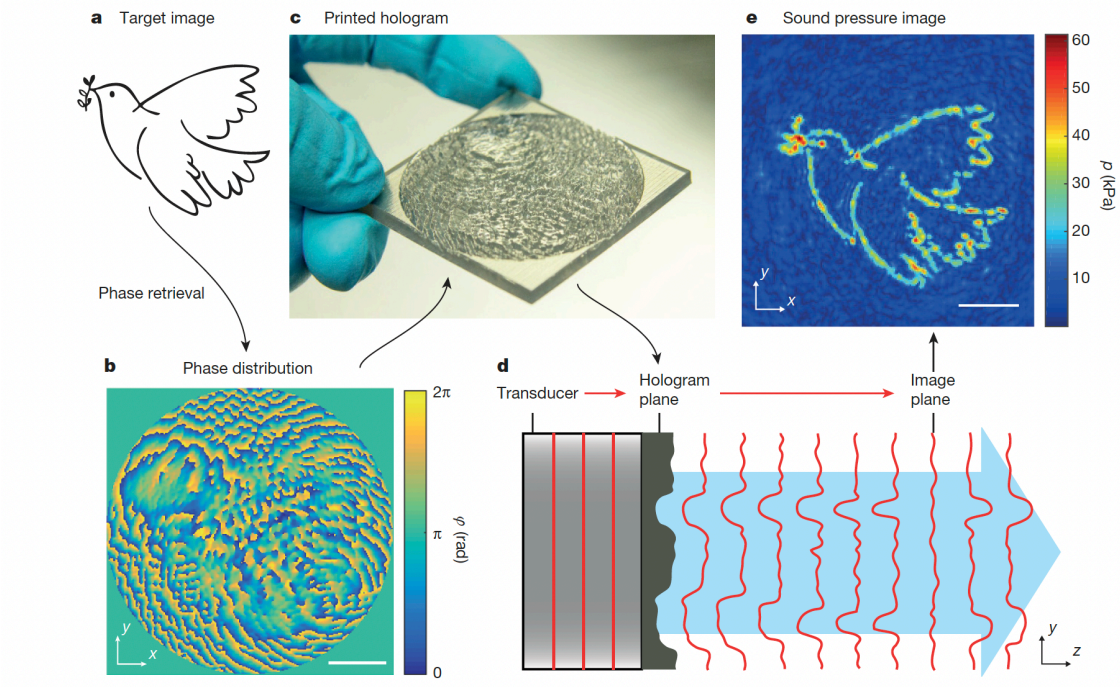


Figure 2.1: Procedure of making a two-dimensional acoustic holograms. Image extracted from [9].

This approach to manipulating the acoustic wavefront offers substantial advantages in therapeutic ultrasound, where accurate targeting of specific brain regions is essential. The considerable acoustic impedance mismatch between the skull and adjacent media introduces phase aberrations that degrade beam quality through refraction and reflection. Holographic lenses provide an effective solution by compensating for these distortions, thereby restoring the coherence of the wavefront and enabling precise energy concentration at the intended focal region. This correction is critical for improving the spatial accuracy and therapeutic efficacy of transcranial ultrasound interventions, particularly in the treatment of neurological conditions.

2.2 Transcranial ultrasound therapy

By engineering lenses capable of concentrating ultrasound energy with high spatial precision in heterogeneous media, the performance of transcranial therapeutic procedures can be significantly improved while reducing collateral effects on surrounding tissues. Ultrasound waves, which are mechanical oscillations transmitted through media like water or biological tissue, deposit part of their energy as heat due to intrinsic viscoelastic damping mechanisms. This thermal conversion is a fundamental principle in many therapeutic applications [25], where the clinical effect is governed by both the peak temperature achieved and the exposure duration.

In imaging applications, ultrasound is used to visualize internal structures—such as organs or tissues—by analyzing the echoes of reflected waves. In these cases, the temperature increase is negligible due to the relatively low energy of the acoustic field [26]. In contrast to diagnostic uses, therapeutic applications of ultrasound employ high-intensity acoustic waves to selectively heat specific tissue regions, thereby inducing biological ef-

fects such as thermal ablation or cell necrosis. Precise control of the focal region is crucial to ensure accurate delivery of acoustic energy to the target, which directly enhances the safety and effectiveness of these treatments. Representative techniques include hyperthermia [27], [28], thermal ablation [29], histotripsy [30], extracorporeal shockwave lithotripsy [31], and blood–brain barrier opening [32], among others.

A promising non-invasive approach for transcranial ultrasound therapy involves the design of acoustic holographic lenses capable of focusing ultrasound waves precisely on specific brain regions [33]. These simulations enable accurate modeling of wave propagation through complex anatomical structures, such as the skull, allowing the creation of patient-specific lenses that compensate for acoustic aberrations and optimize energy delivery at the focal point. Previous research has demonstrated that holographic lenses can significantly improve the precision and efficiency of transcranial ultrasound therapies [34]. Typically, such lenses are coupled with a medium like water to facilitate efficient wave transmission toward the target region. However, this setup is frequently unsuitable for clinical use due to its complexity and limited feasibility in real-world scenarios.

The present study introduces the design of an acoustic lens that can be directly positioned on the patient's scalp, enhancing both its clinical applicability and the acoustic coupling between the lens and the anatomical surface. Numerical simulations are performed to evaluate the performance of the proposed lens design, with special focus on how different material combinations affect wave propagation and focusing efficiency.

Chapter 3

Materials and methods

3.1 Materials

The interaction between ultrasound waves and biological tissues is strongly governed by the acoustic properties of the materials they traverse. In the context of this study, three primary components are involved in the acoustic path: the patient's skull, the piezoelectric transducer serving as the ultrasound source, and the material of the lens that shapes the wavefront. Accurate knowledge of these elements is essential for realistic simulation of wave propagation and for designing a lens capable of achieving precise focusing.

This work investigates a bidirectional holographic lens designed for direct application to the patient's scalp. To assess its performance, various material combinations are tested to study how ultrasound waves interact with both the patient's head and the lens. Before delving into the design methodology, it is necessary to characterize the physical and acoustic parameters of all media involved. This step is fundamental to ensure accurate modeling of the acoustic field and to define the boundary conditions required for lens op-

timization. The following section outlines the materials used in the simulations, including the ex vivo human skulls, the candidate materials for the lens and coupling medium, and the specifications of the ultrasound transducer used for forward propagation.

3.1.1 Skull

The human skull is a complex anatomical structure composed of multiple bone regions that protect the brain and provide mechanical support. The study is performed over three different *ex vivo* patients employed to simulate the interaction between ultrasound waves and cranial tissues. These samples are provided by the *Ultrasound Medical and Industrial Laboratory* (UMIL), part of the *Instituto de Instrumentación para Imagen Molecular* (I3M) department at the *Universitat Politècnica de València* (UPV).



Figure 3.1: Ex-vivo skull sample used in the simulations. The samples are provided by the UMIL laboratory, part of the I3M department at the Universitat Politècnica de València.

High-resolution computed tomography (CT) scans, with a spatial resolution of $0.6621 \times 0.6250 \times 0.6621$ mm^3, are used to extract the skull's acoustic properties by leveraging the linear relationship between X-ray attenuation values and tissue composition. From the CT

images and the linear relationship between X-ray attenuation values, the speed of sound and density of hard and soft tissues are estimated using empirical models that relate Hounsfield Units (HU) to key acoustic parameters. This approach enables a realistic simulation of ultrasound wave propagation through the heterogeneous structure of the skull. The specific relationship applied depends on whether the tissue is classified as soft or bone, following the experimental data reported by Schneider [35] and the empirical model proposed by Mast [36]. This relationship is illustrated in Figure 3.2.

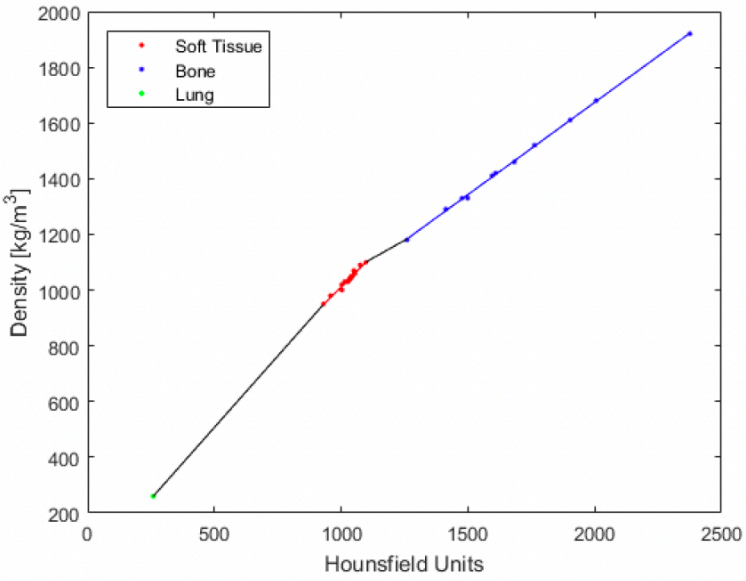


Figure 3.2: Lineal relationship between Hounsfield Units (HU) and density. The relationship is defined for both soft and bone tissues, as described in [35] and [36].

To assess the robustness and adaptability of the lens design, three different skull samples with varying anatomical characteristics are considered. This enables a comprehensive evaluation of the system's performance under inter-subject variability and across different cranial geometries.

3.1.2 Transducer

In ultrasonic applications, wave generation is typically achieved using piezoelectric transducers, which convert electrical energy into mechanical vibrations that produce acoustic waves. This process is based on the inverse piezoelectric effect, a property of certain solids—typically crystals and ceramics—that causes them to deform mechanically when an electric voltage is applied across their surfaces. As the material vibrates in response to the electrical signal, it generates pressure waves at ultrasonic frequencies.

The source used in this study is a flat circular transducer working at a central frequency of $f_0 = 560$ kHz, with an aperture of 65 mm. The transducer is positioned at a distance of 30 mm respect the skull's calvaria, with an orientation ensuring that the emitted wavefront effectively converges at the target region.

3.1.3 Lens and coupling material

The lens and coupling medium are fundamental components in the design of the holographic system, as they directly influence the propagation of ultrasound waves toward the target region. The materials selected for these components are chosen based on their acoustic properties, which must be compatible with the transducer and optimized for efficient wave transmission.

The main objective of this study is to develop a composite holographic lens composed of two different materials: one for the lens matrix and another for the coupling medium. This dual-material design enables a systematic analysis of how various combinations influence ultrasound wave propagation through both the lens and the skull, with a particular focus on wave intensity and focal performance. To this end, two types of materials are in-

vestigated. The first is acoustically soft, characterized by a lower acoustic impedance than water, while the second is acoustically hard, with a higher impedance. These materials are evaluated in a water-based medium in order to determine their respective impacts on transmission efficiency and focal quality.

The soft material is a silicone, specifically *Elite Double 8*, from the Zhermack laboratory. This is a commercially available silicone rubber commonly used for abutment duplications due to its low hardness (8 Shore A), high elasticity, and excellent detail reproduction. This material is chosen for its ability to conform to the irregular shape of the skull, ensuring effective coupling with the transducer. The hard material used in this study is a photopolymer resin—*Clear Resin* from Formlabs, referred to as *plastic* throughout this work—which is commonly used in high-precision 3D printing applications. Its acoustic properties, such as sound speed and density, were experimentally characterized in our laboratory [38] and are summarized in Table 3.1.

Table 3.1: Acoustic properties of the materials used for the lens, coupling medium, and reference.

Material	**Speed of Sound** c [m/s]	**Density** ρ [kg/m^3]	**Absorption** [dB/(cm $\cdot$ MHz)]
Soft	973.6	920	2.95
Hard	2600	1186	3.27
Water	1500	1000	0.00[a]

[a]Absorption in water is computed using the `waterAbsorption` function from the `k-Wave` toolbox [37].

These two materials are combined with water in various configurations to create the lens and coupling medium matrices as illustrated in Figure 1.1. The goal is to assess how different material pairings affect the propagation of ultrasound waves through the lens and skull in terms of intensity and focusing characteristics.

3.2 Modeling of the acoustic field

Numerical simulations are conducted using the `k-Wave` toolbox [37], [39] to model the propagation of acoustic waves through heterogeneous media. This methodology enables the reconstruction of complex wavefronts capable of precisely focusing acoustic energy at the desired target, despite the distortions introduced by intervening tissue layers. The acoustic field is computed based on the physical properties of the materials involved—including the lens, the coupling medium and the skull. Calculations are performed using the pseudospectral time-domain (PSTD) method, a numerical technique that allows efficient simulation of pressure fields in absorbing and heterogeneous media. Compared to the more commonly used finite-difference time-domain (FDTD) method, the PSTD approach offers improved computational efficiency by allowing the use of coarser spatial and temporal grids, thereby reducing the required number of points per wavelength.

The PSTD provides a numerical solution to a system of three coupled first-order partial differential equations in a heterogeneous medium, comprising the continuity equation, the momentum conservation equation, and the pressure–density relationship.

$$\frac{\partial \rho}{\partial t} = -\rho_0 \nabla \cdot \vec{v} - \vec{v} \cdot \nabla \rho_0 \tag{3.1}$$

$$\frac{\partial \vec{v}}{\partial t} = -\frac{1}{\rho_0} \nabla p \tag{3.2}$$

$$p = c^2 \left(\rho + \vec{d} \cdot \nabla \rho_0 - \mathbf{L}\rho \right) \tag{3.3}$$

where ρ_0 denotes the ambient density of the medium, ρ represents the acoustic density perturbation, and p corresponds to the acoustic pressure. The parameter c is the speed of sound in the medium, while $\vec{v}$ is the velocity field induced by the acoustic wave. The term

$\vec{d}$ stands for the particle displacement vector, and $\mathbf{L}$ is an integro-differential operator that models the frequency-dependent acoustic absorption and dispersion.

The absorption effect in biological tissues is modeled using a frequency-dependent attenuation law, defined by the empirical relationship:

$$\alpha(f) = \alpha_0 \cdot f^y, \tag{3.4}$$

where $\alpha(f)$ is the attenuation coefficient in Np/m at frequency f (in Hz), α_0 is a material-specific constant with units Np/m/Hz, and y is an exponent that characterizes the frequency dependence of attenuation for the tissue type. Both values, α_0 and y are obtained from IT'IS database [40] for the brain and skull tissues. According to this, the value of y is assumed to be 1 in the absence of detailed measurements. This formulation provides a more realistic representation of ultrasonic energy loss in tissue, capturing the dispersive and absorptive behavior of biological media.

To simulate the complete lens design process and assess its performance, the Pseudospectral Time-Domain (PSTD) method is employed to solve the full set of acoustic equations in the time domain across one, two, or three dimensions using a spatial frequency (k-space) representation. The acoustic pressure field is computed at each point in the domain by discretizing the wave equations according to the material properties of the media involved. This numerical framework also allows for the incorporation of mass and force source terms directly into the discretized equations, as well as the use of an anisotropic absorbing boundary layer—known as a Perfectly Matched Layer (PML)—which minimizes undesired reflections from the domain boundaries and enables realistic simulation of wave propagation in open media.

3.3 Holographic lens design

To determine the optimal wavefront required for accurate focusing, simulations of the acoustic field emitted by a virtual source located at the target position are first conducted. The resulting wavefront is recorded at the lens plane and serves as the basis for designing the holographic lens. This approach enables the lens to be engineered with a spatially varying distribution that modulates both the phase and amplitude of the incoming acoustic field. As a result, the reconstructed wavefront can concentrate acoustic energy precisely at the intended focal point, even in the presence of heterogeneous media such as bone. This tailored modulation ensures reliable control of the focal region in both homogeneous and inhomogeneous environments, including biological tissues, where complex geometries and variable acoustic properties can introduce significant aberrations in the ultrasound wavefront [11].

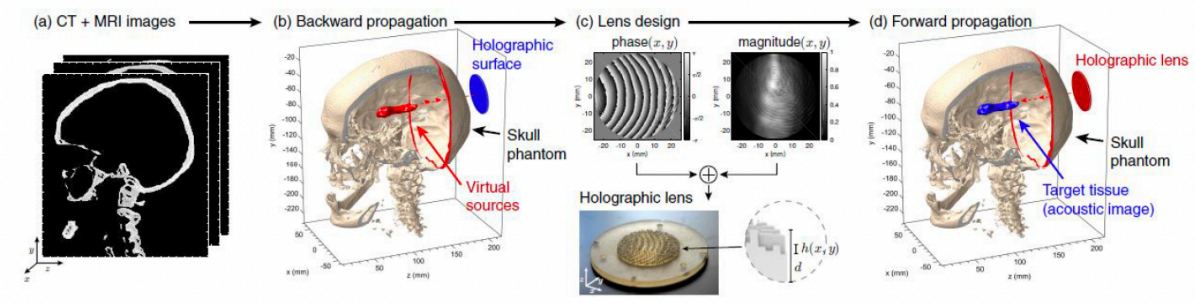


Figure 3.3: Hologram generation process: (a) CT/MRI images. (b) Therapeutic target acting as a virtual source of acoustic waves (red) and holographic recording surface (blue). (c) Lens design. (d) Ultrasound propagation from the transducer through the entire medium. Diagram obtained from [11].

Following the acquisition of the patient's anatomical data via CT imaging, the lens design process employs backward acoustic propagation, in which the resulting wavefront is recorded at the lens plane. This field is then complex-conjugated to obtain a time-reversed

version at the desired frequency. Phase information is preserved, as it contains the critical encoding needed to design the holographic lens.

3.3.1 Lens design

The analysis focuses on how different material combinations used in the construction of the acoustic lens influence ultrasound wave propagation. A virtual source is modeled as a point emitter located at a fixed position relative to the transducer, generating wavefronts that travel through the propagation medium, including the holographic lens and the skull. These wavefronts are captured on a predefined holographic plane, $\mathbf{r}_0 = (x_0, y_0, z_0)$, defined in a Cartesian coordinate system.

The height profile of the lens is derived from the phase distribution of the wavefront recorded at each pixel on the holographic plane. The lens is designed to be coupled to a single-element transducer, and each pixel on the plane locally modifies the phase of the incident wavefront. Consequently, the lens can be understood as an array of square pixels with uniform lateral dimensions but varying heights [41]. Assuming that each pixel behaves as a longitudinally oscillating elastic Fabry–Pérot resonator, the complex, frequency-dependent transmission coefficient of each pixel, evaluated at the holographic plane, is given by

$$T = \frac{2Z_n e^{-ik_0(d-h)}}{2Z_n \cos(k_L h) + i(Z_n^2 + 1)\sin(k_L h)}, \tag{3.5}$$

where $Z_n = \frac{Z_L}{Z_0}$ denotes the normalized acoustic impedance, $Z_0 = \rho_0 c_0$ and $k_0 = \frac{\omega}{c_0}$. The quantities ρ_0, c_0, and $Z_L = \rho_L c_L$, with $k_L = \frac{\omega}{c_L}$, correspond to the density, sound speed, and acoustic impedance in the filling media and in the lens material, respectively.

Since Equation 3.5 contains trigonometric functions, it cannot be inverted analytically to obtain the height of each lens pixel. As a result, a numerical approach is used, evaluating the equation over a defined range of pixel heights from the base of the lens to a maximum limit. The objective is to determine the pixel height that produces a transmission coefficient 2π greater than that at the lens's minimum height. Once this dataset is generated, interpolation is applied to estimate the pixel height that most closely achieves the target phase. This process is repeated for each pixel on the holographic plane, resulting in a height profile that defines the lens geometry.

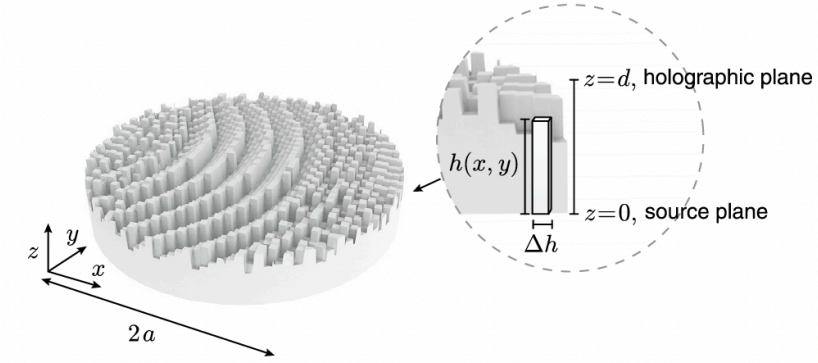


Figure 3.4: Height profile of the lens: with an aperture of $2a$ and is divided into pixels, each defined by a height function $h(x, y)$. The acoustic source is positioned at $z = 0$, while the plane where the hologram is encoded lies at a distance $z = d$.

Focusing on lens development adapted to human cranial anatomy, this study ensures the use of a consistently planar holographic surface for accurate wavefront reproduction. Some of the lenses presented are designed for direct placement on the skull surface, while others are intended to be positioned within a water medium to facilitate effective ultrasound propagation through the lens toward the target region.

3.3.2 Generated acoustic fields

Forward simulation serves to validate whether the lens correctly concentrates the ultrasound energy at the desired focal region. This involves simulating the wavefront emitted by a transducer as it passes through the lens and confirming its convergence at the intended focal point, which corresponds to the location of the virtual source. The simulation takes into account the acoustic properties of the lens materials, as well as the wave distortions caused by skull-induced aberrations.

Simulating the acoustic field in *k-Wave* requires defining four input structures: the grid, medium, source, and sensor. The grid structure determines the spatial discretization of the computational domain, specifying both the number of points in each dimension and the spatial step size. The medium structure defines the acoustic properties of the materials involved. The source structure describes the characteristics of the virtual source. Lastly, the sensor structure defines the locations within the computational domain where the acoustic pressure field is recorded during the simulation.

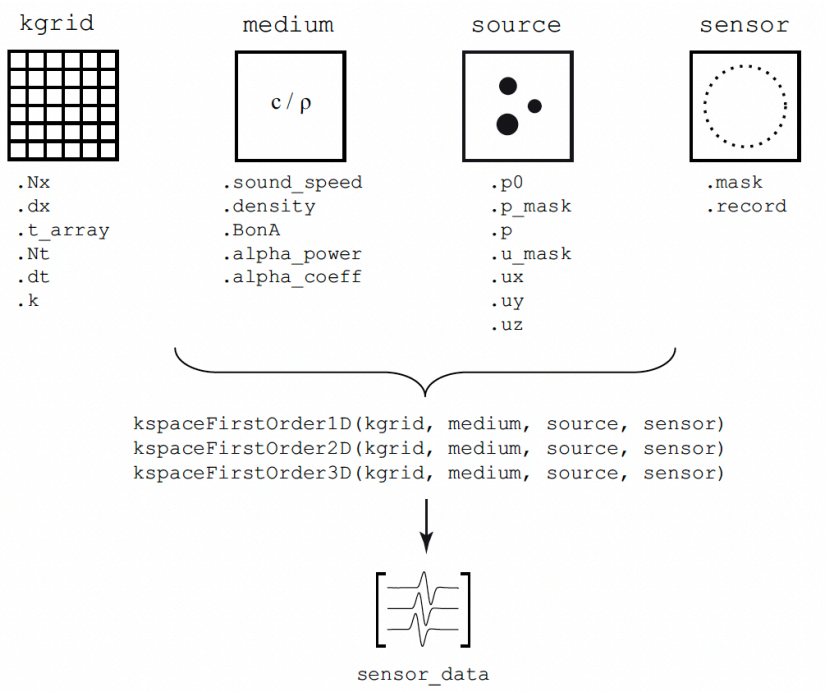


Figure 3.5: Structure of k-Wave inpucts functions. Diagram obtained from [37].

Computational grid

The computational grid defines how the medium is divided into a mesh of grid points and how the acoustic field is discretized within the computational domain. It can be understood as the resolution of the simulation. Each grid point represents a discrete location where the governing equations are solved. The grid is specified by the number of points in each dimension, N_x, N_y, and N_z, and by the spatial step sizes, dx, dy, and dz, along the Cartesian axes, which determine the distances between adjacent grid points. The resolution must be fine enough to accurately capture the propagation of acoustic waves, yet not so fine that it renders the simulation computationally impractical.

Resolution is governed by the wavelength of the ultrasound waves and the spatial step size, which must be sufficiently small to accurately model wave behavior at the given

operating frequency. To ensure numerical stability and accurate modeling of wave propagation, the spatial step size is commonly chosen as one-sixth of the wavelength. This condition can be expressed as:

$$\Delta s = \frac{c_0}{6 f_0}, \tag{3.6}$$

where $\Delta s = dx = dy = dz$ are the resolution in each axis, c_0 is the speed of sound in the medium and f_0 is the central frequency of the ultrasound wave.

The total dimensions of the computational grid must also be defined and converted into the corresponding number of points along each spatial dimension. The overall size of the grid is determined by the dimensions of the skull and the additional space required to accommodate both the lens and the transducer within the simulation domain. Specifically, grid sizes multiple of low number of prime factors are preferred, as they allow for reducing the computational time execution of operations, such as those used in pseudospectral methods.

Once the original CT image is loaded—with known spatial resolution along each axis—the grid is interpolated to satisfy the spatial sampling condition defined by the acoustic wavelength. The number of grid points along each axis is then calculated based on the interpolated physical size of the domain and the selected spatial step size. For instance, in the z-axis:

$$N_z = \frac{z}{\Delta s}, \tag{3.7}$$

where z denotes the interpolated physical length of the domain in the z-direction, and Δs is the spatial step size chosen according to the resolution criterion.

This relationship is applied to each spatial dimension, resulting in the total number of grid points that define the computational domain. The grid structure is thus specified by

these parameters and the chosen spatial step size, creating a uniform discretization of the space in which the acoustic field will be simulated.

Medium properties

The medium structure defines the spatial distribution of acoustic properties within the heterogeneous media considered in the simulation. These properties obtained from the CT images include the speed of sound, measured in $[\,\mathrm{m/s}\,]$; density, measured in $[\,\mathrm{kg/m^3}\,]$; and the acoustic absorption parameters, such as the absorption coefficient, expressed in $\mathrm{dB/(cm \cdot MHz^y)}$, and the frequency power law exponent y. These parameters are essential for accurately modeling wave propagation through the medium. Depending on the materials used for both the lens and the surrounding medium, the domain is defined either as a heterogeneous or homogeneous medium. In the heterogeneous case, each grid point can take different acoustic parameters to reflect local variations—such as in the skull, where distinct regions are assigned specific values based on their physical composition. Conversely, if the surrounding environment is acoustically uniform, like water, it can be modeled as a homogeneous medium. The acoustic properties of the medium are defined in a matrix format, where each element corresponds to a specific grid point in the computational domain.

Several simulations were carried out to evaluate the influence of different materials and configurations assigned to the coupling medium and lens matrices on ultrasound wave propagation. The objective is to identify the optimal combination of materials that ensures efficient wave transmission while reducing aberrations induced by the skull. A total of six configurations were tested, combining three different materials—water, silicone, and resin—assigned to the coupling medium and lens matrices. Each simulation assesses a specific pairing of materials in both matrices to determine the characteristics of each

configuration and its impact on the focusing performance of the lens.

Source definition

The source is the component responsible for emitting the acoustic signal. In this study, two distinct sources are defined. The first is a virtual source, used during the backward propagation process to compute the desired phase and amplitude distribution for lens design. The second is a physical transducer source, employed in the forward propagation simulation to generate the actual acoustic field.

The virtual source is modeled as a point source positioned 65 mm away from the transducer. This study does not aim to investigate the ability to focus on arbitrary regions within the brain. Instead, it is specifically designed to focus precisely on a single target point, in accordance with the comparative approach adopted in this work. This virtual source emits an acoustic wavefront that propagates through the medium, including the lens and the skull, and is subsequently recorded on the holographic plane. This source operates at a central frequency of $f_0 = 560$ kHz, emitting a spherical, sinusoidal wave composed of 100 cycles. This generates a stationary wave pattern that propagates both forward and backward, allowing the capture of the modified wavefront resulting from interactions with the lens and the skull.

Conversely, the transducer source acts as the in the forward simulation. It is modeled as a circular, planar transducer with all points vibrating at the same amplitude and frequency, f_0. The transducer is emitting a spherical wavefront that travels through the medium, including the lens and the skull, and is recorded by the sensor array defined in the simulation.

Sensor definition

The sensor is the component used to record the acoustic wavefront during the simulation. In this study, in backward simulation is defined as a flat, planar array of points parallel to the transducer surface and with matching dimensions. This sensor is positioned on the holographic plane, located between the virtual source and the transducer, and is responsible for capturing the acoustic pressure field required for the backward propagation process and lens design. In the forward simulation, the sensor is defined over the entire computational grid, allowing full-field recording of the acoustic wave propagation throughout the domain.

3.4 Study design

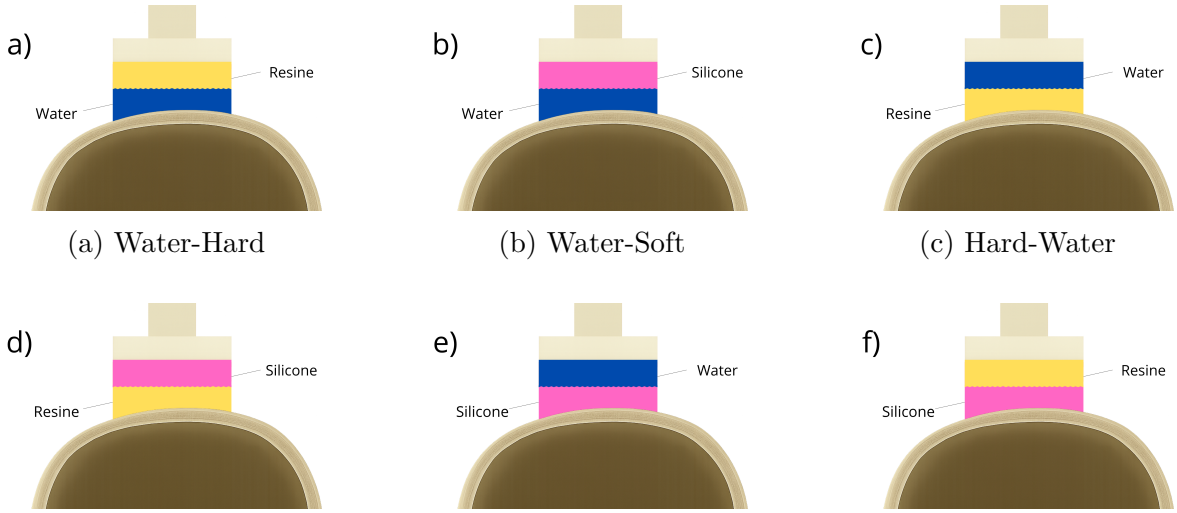
The study is based on a series of numerical simulations aimed at evaluating the performance of different material combinations used in the lens and coupling medium matrices. The primary objective is to compare the efficiency of ultrasound wave propagation across configurations using quantitative metrics, with the goal of minimizing skull-induced aberrations and enhancing the focusing capability of the holographic lens.

3.4.1 Study configuration

To evaluate the performance of different acoustic materials in a water-based environment, six distinct configurations have been defined. Each configuration combines two materials: one for the lens matrix and the other for the coupling medium. The soft material, shown in pink, is silicone, while the hard material, displayed in yellow, is resin. The properties of both materials are detailed in Section 3.3.2. Water, represented in blue, serves as the

surrounding medium between the transducer and the lens, providing acoustic coupling for efficient wave transmission in some of these configurations.

In previous studies, the coupling medium has typically been defined as water, given its favorable acoustic properties and widespread use in transcranial ultrasound applications. However, in the present study, two alternative coupling media are introduced to assess how different material compositions affect ultrasound wave propagation and focusing performance in the design of a bi-directional lens, as illustrated in Figure 3.5. The first alternative is silicone, which is used as the coupling medium in two configurations [Figure 3.5(e) and 3.5(f)], while the second is resin, employed in configurations [Figure 3.5(c) and 3.5(d)]. The remaining two configurations use water as the coupling medium [Figure 3.5(a) and 3.5(b)], following the traditional approach and serving as a baseline for comparison.



(a) Water-Hard (b) Water-Soft (c) Hard-Water

(d) Hard-Soft (e) Soft-Water (f) Soft-Hard

Figure 3.6: Six different configurations of the lens and coupling medium matrices. Each configuration combines two materials: first for the coupling and second for the lens matrix.

The different configurations are evaluated to investigate how the choice of materials influences ultrasound wave propagation through the skull, as well as the overall focusing performance at the target point, measuring the pressure amplitude at the whole sensor array.

3.4.2 Metrics

To quantitatively evaluate the performance of the different material combinations used in the lens design, several key parameters are extracted from the results of the numerical simulations. These parameters include the acoustic gain, focal deviation, depth of focus and full width at half maximum (FWHM). Each of these metrics is computed for every configuration and skull sample, providing detailed insight into the lens's focusing performance and its ability to concentrate ultrasound energy at the intended focal spot. The results obtained from these metrics are associated with an uncertainty, which is estimated by conducting simulations on three different ex-vivo skull samples. The uncertainty is quantified as the standard deviation of the metric values obtained across the three skulls, providing a statistical measure of the robustness and consistency of each configuration.

Gain

The acoustic gain G is defined as the ratio between the maximum absolute acoustic pressure amplitude $|p|$ obtained at the focal point and the initial pressure amplitude p_0 emitted by the virtual source. It enables a direct comparison between the initial emitted pressure and the resulting pressure after wave propagation through the lens and the skull. The gain therefore quantifies the amplification effect induced by the lens design, and is math-

ematically expressed as:

$$G = \frac{|p|}{p_0} \tag{3.8}$$

Physically, the gain can be interpreted as a measure of the acoustic intensity at the focal point, relative to the initial pressure generated by the virtual source. The acoustic intensity I, defined as the average power transmitted per unit area, is given by:

$$I = \frac{p_0^2}{2\rho_0 c_0} \quad [\mathrm{W/m^2}] \tag{3.9}$$

where p_0 is the acoustic pressure amplitude, ρ_0 is the density of the medium, and c_0 is the speed of sound in that medium.

In this study, as the gain is compared across different material configurations, the intensity cannot be directly inferred from the pressure amplitude alone, since the acoustic impedance, Z, varies depending on the materials used in the lens and the coupling medium. Therefore, it is necessary to normalize the gain with respect to a reference case in which the coupling medium is water, commonly used in transcranial ultrasound applications. To account for the differences in acoustic impedance between the tested materials and the reference medium (water), a correction factor α is introduced. This factor normalizes the gain across different configurations, enabling a fair comparison of acoustic performance not biased by differences in propagation media and isolating the effect of lens and coupling material configurations. The correction factor is defined as:

$$\alpha = \sqrt{\frac{Z_\mathrm{L}}{Z_\mathrm{w}}} \tag{3.10}$$

where $Z_\mathrm{L} = \rho_\mathrm{L} c_\mathrm{L}$ is the acoustic impedance of the tested lens material, and $Z_\mathrm{w} = \rho_\mathrm{w} c_\mathrm{w}$ is the acoustic impedance of water.

The corrected acoustic gain G_{norm} is then obtained by multiplying the raw gain G by this factor:

$$G_{\text{norm}} = G \cdot \alpha = \frac{|p|}{p_0} \cdot \alpha \tag{3.11}$$

Focal deviation

The focal deviation Δd quantifies the spatial displacement between the actual and intended focal point. It is defined as the Euclidean distance between the point of maximum acoustic pressure amplitude obtained from the simulation and the predefined position of the virtual source, which serves as the reference for ideal focusing. Mathematically, it is given by:

$$\Delta d = \sqrt{(x_{\max} - x_0)^2 + (y_{\max} - y_0)^2 + (z_{\max} - z_0)^2} \tag{3.12}$$

where $(x_{\max}, y_{\max}, z_{\max})$ are the coordinates of the observed focal point, and (x_0, y_0, z_0) are the coordinates of the virtual source (target focus). The focal deviation provides a measure of how accurately the lens design can focus the ultrasound energy at the desired focal spot. A smaller focal deviation indicates better focusing performance, while a larger deviation suggests that the lens design is not effectively concentrating the acoustic energy at the intended target.

Depth of Focus (DOF) and Full Width at Half Maximum (FWHM)

The *Depth of Focus* (DOF) and the *Full Width at Half Maximum* (FWHM) are two complementary metrics that describe the spatial confinement of acoustic energy around the focal point. Together, they characterize the three-dimensional focusing performance of an ultrasound beam.

The DOF quantifies the beam's axial extent along the propagation direction—specifically, the z-axis—over which the pressure amplitude remains above half its maximum value (i.e., within the -6 dB level). This measure is particularly important in therapeutic applications, as it indicates the volume along the beam's axis where sufficient acoustic intensity is maintained for effective energy delivery. It reflects the beam's capability to remain focused over a depth range rather than at a single point.

In contrast, the FWHM characterizes the lateral confinement of the beam in the plane perpendicular to the propagation direction—typically the xy-plane. It is defined as the distance between the two points along the x- and y-axes where the pressure amplitude also drops to 50% of the maximum value. This metric provides insight into the beam's lateral resolution and how precisely the energy is concentrated across the transverse plane.

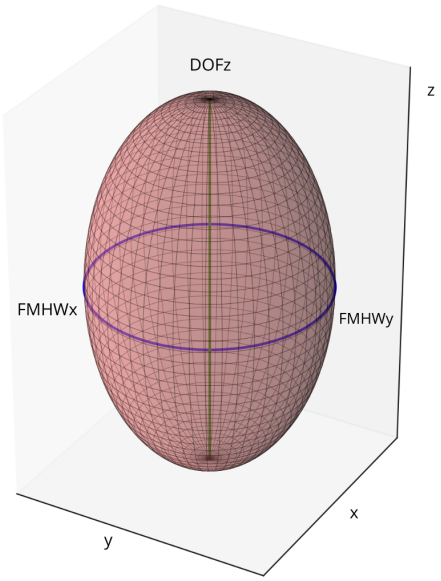


Figure 3.7: Graphical representation of the spatial focusing parameters evaluated from the simulated acoustic field: $FWHM_x$, $FWHM_y$, and DOF.

Chapter 4

Results

This comparative analysis offers meaningful insights into the ability of each configuration to correct skull-induced acoustic aberrations and to accurately focus energy at the intended target region.

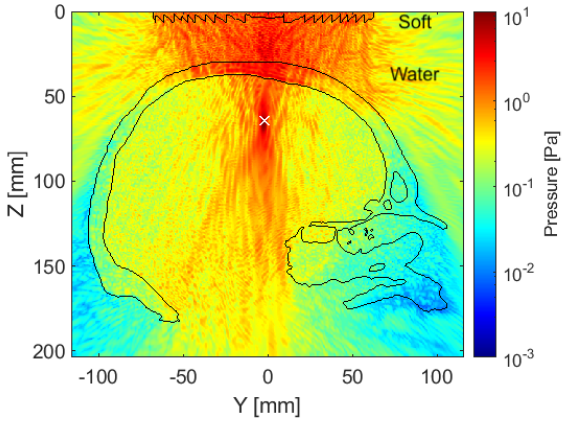
4.1 Pressure distribution at the focal point

For illustrative purposes, the following results display the acoustic pressure at the focus for Subject 1, exemplifying the behavior of each tested configuration. The results are shown through 2D cross-sectional views of the acoustic field, complemented by 1D line profiles along the principal axes. These visualizations offer both qualitative and quantitative perspectives on how different material combinations influence the lens's focusing performance. The cross-sectional maps reveal the spatial extent and shape of the focal region, while the 1D profiles along the X, Y, and Z axes allow for a detailed comparison of pressure amplitude, focal sharpness, and localization across all configurations. The val-

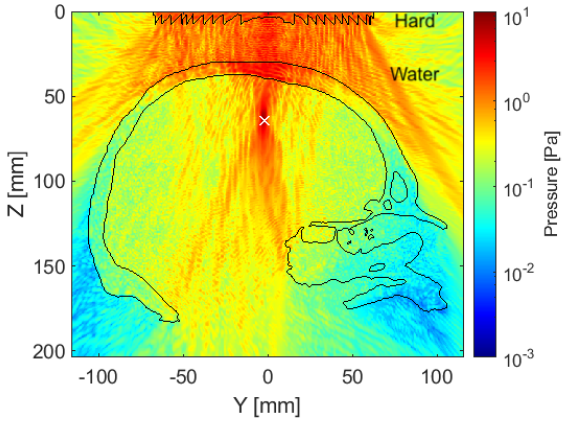
ues are expressed in units of P/P_0, where P_0 denotes the peak pressure emitted by the transducer.

4.1.1 2D visualization of the acoustic pressure field

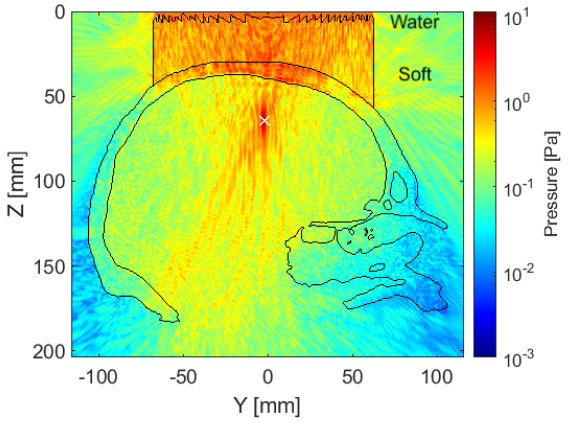
Figure 4.1 presents a 2D cross-sectional view of the acoustic pressure field in the yz-plane at the focal depth, illustrating the performance of the holographic lens for each of the six tested material configurations. The simulation corresponds to one of the three skull samples, which is fully immersed in a water environment. Each subfigure represents a specific combination of coupling medium and lens material. A colormap is used to display the normalized pressure amplitude, where warmer tones represent higher acoustic pressure levels.



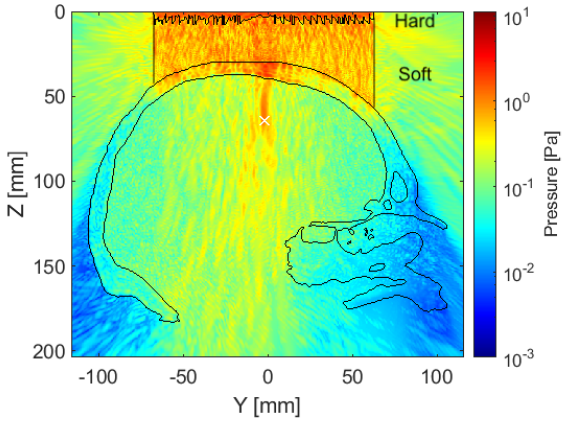
(a) Water - Soft



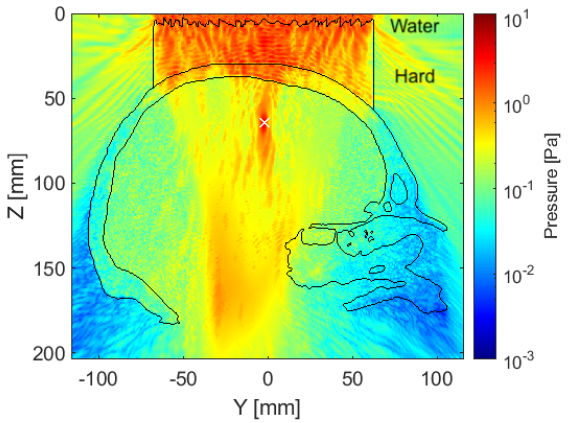
(b) Water - Hard



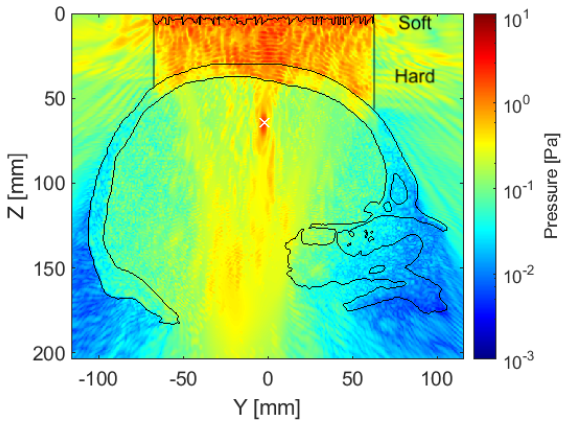
(c) Soft - Water



(d) Soft - Hard



(e) Hard - Water



(f) Hard - Soft

Figure 4.1: **Skull Sample 1.** Pressure distribution at the focal point for each configuration.

The focal region is visually identifiable across all configurations; however, noticeable differences arise in both peak intensity and the apparent extent of energy concentration. Even though only one skull sample is presented, the qualitative behavior of the pressure distribution is consistent across all three skulls.

Configurations in which water acts as a coupling medium exhibit more prominent focal zones with higher pressure amplitudes. This behavior is likely attributable to the lower overall acoustic attenuation due to the presence of water. In particular, the *Water–Soft* configuration—comprising only low-impedance materials—produces a sharply defined and intense region of energy deposition. Similarly, the *Water–Hard* case results in a distinct high-pressure area, albeit with slightly reduced magnitude, suggesting some influence of the resine high-impedance layer. In contrast, configurations involving transitions between soft and hard materials (e.g., *Soft–Hard* and *Hard–Soft*) display more dispersed energy distributions with notably lower pressure amplitudes. The *Soft–Water* and *Hard–Water* configurations demonstrate intermediate focusing behavior. Although their peak pressures are lower and the focal regions appear less well defined than those of coupling water-based configurations, they still retain some degree of localized energy concentration. The presence of a solid coupling medium introduces moderate impedance mismatch and wavefront distortion, while the internal water layer may help partially recover focal quality.

4.1.2 1D line profiles of the acoustic field

To complement the 2D visualization of the acoustic pressure field, one-dimensional (1D) line profiles were extracted along the principal Cartesian axes intersecting the focal point. These transverse profiles provide quantitative insight into the spatial distribution and confinement of the acoustic energy along each direction. By analyzing the pressure magnitude along individual spatial dimensions, it becomes possible to evaluate the peak pressure,

quantify the deviation from the intended focal position, and characterize the overall shape of the pressure distribution.

The 1D line profiles are presented in Figures 4.2, 4.3 and 4.4 for the X, Y, and Z axes, respectively. Each figure shows the pressure distribution for skull sample 1 across all the configurations. The transverse field in X-axis and Y-axis are oriented along the lateral direction and the Z-axis one corresponds to the axial direction of propagation.

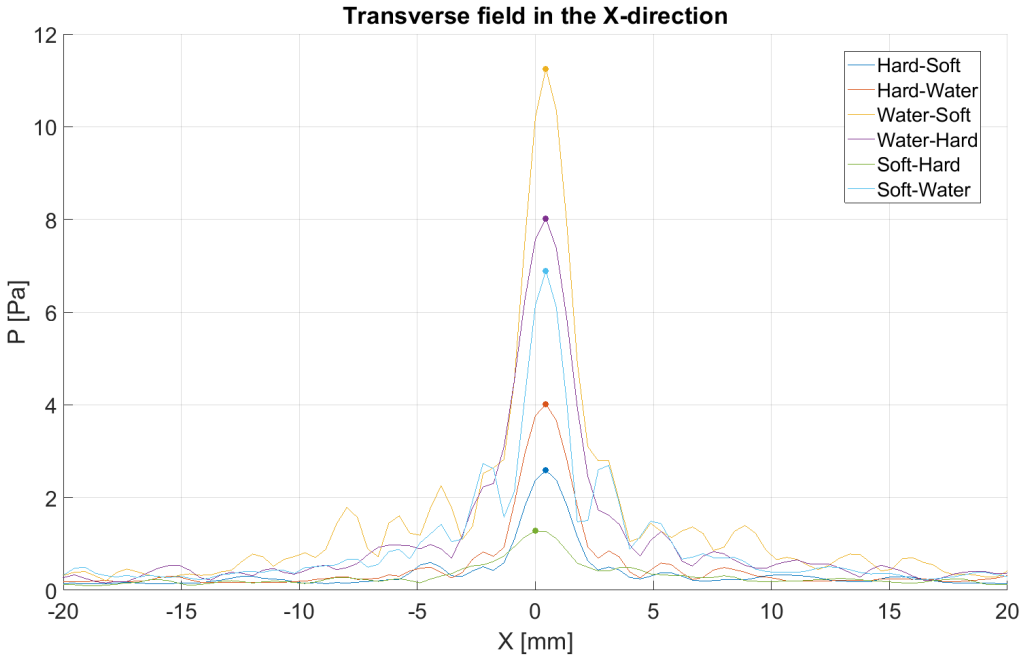


Figure 4.2: Transverse field in X-axis for skull sample 1.

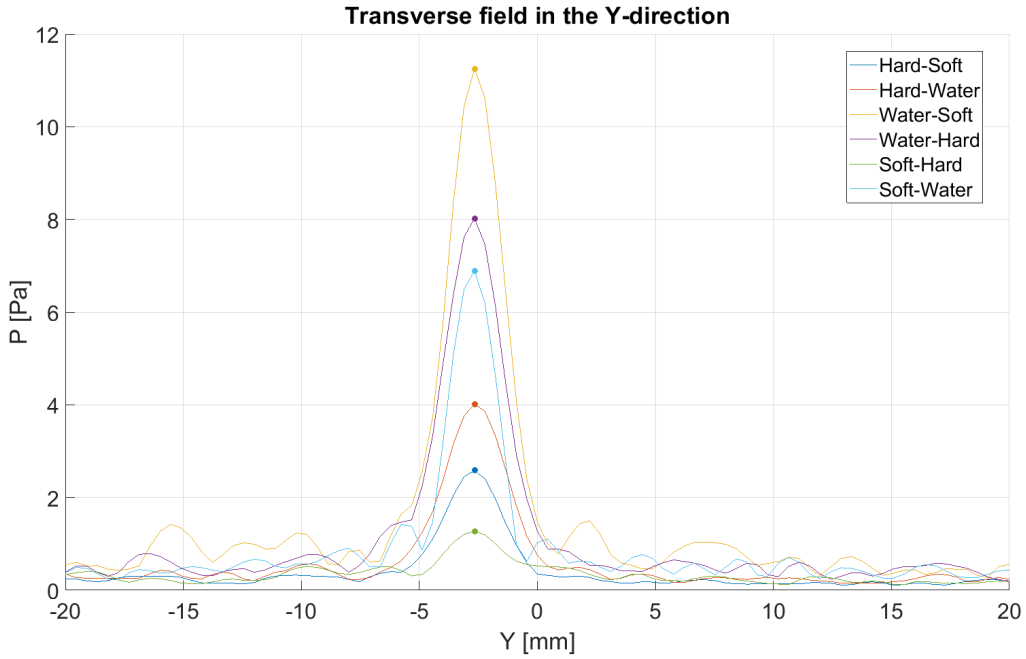


Figure 4.3: Transverse field in Y-axis for skull sample 1.

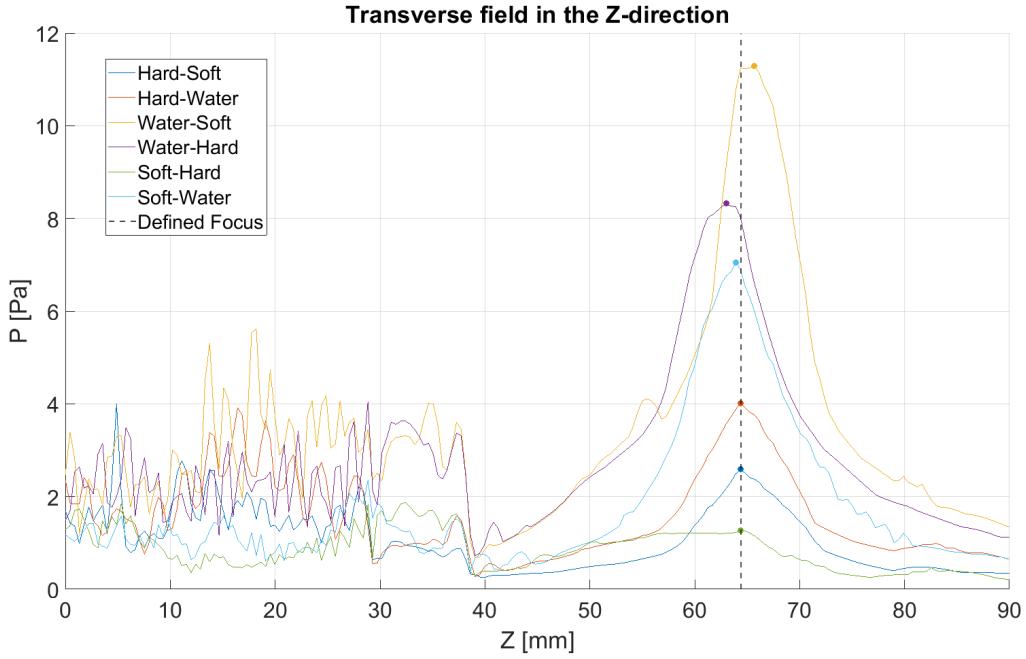


Figure 4.4: Transverse field in Z-axis for skull sample 1.

Consistent with the 2D pressure maps, the transverse field in X and Y-axis reveal well-defined peaks at the focal point, accompanied by symmetrical lateral profiles. The amplitude and sharpness of these peaks vary substantially across the six experimental configurations, reflecting the influence of acoustic impedance mismatches and phase distortions. Across all lateral transverse fields, the *Water–Soft* configuration consistently exhibits the highest peak pressure amplitudes, indicative of superior wavefront coherence and minimal aberration. The *Water–Hard* configuration also achieves high focal pressures, slightly lower, suggesting moderate phase distortion introduced by the hard inner layer. *Soft–Water* and *Hard–Water* configurations result in intermediate peak values, with partial degradation of the focal gain likely due to mismatch at the skull interface. In contrast, *Soft–Hard* and *Hard–Soft* cases yield the lowest peak pressures, pointing to substantial wavefront distortion and acoustic scattering effects induced by the heterogeneous medium transitions.

In the transverse field in Z-axis, the pressure profiles provide additional information on the depth-wise energy localization. In configurations involving transitions between materials with mismatched impedances—particularly *Soft–Hard* and *Hard–Soft*—multiple local maxima are observed upstream of the intended focus. This indicates that the acoustic lens fails to properly converge the wavefront at the target depth, resulting in focal elongation and diminished peak amplitude. Conversely, the *Water–Soft* configuration exhibits a sharply localized and dominant peak close to the original focal point, place where the virtual source was located, across all three skulls, confirming not only superior depth focusing performance but also accurate alignment with the intended focal plane.

4.2 Quantitative analysis of the lens performance

The quantitative evaluation of the holographic lens performance is conducted by extracting the key metrics described in Section 3.4 from the acoustic pressure field at the focal region for each material configuration.

4.2.1 Acoustic gain

The acoustic gain computed from the simulation is presented in Figure 4.5. The corresponding numerical values for each configuration are provided in Table 4.1, offering a comprehensive comparison of the transmission efficiency.

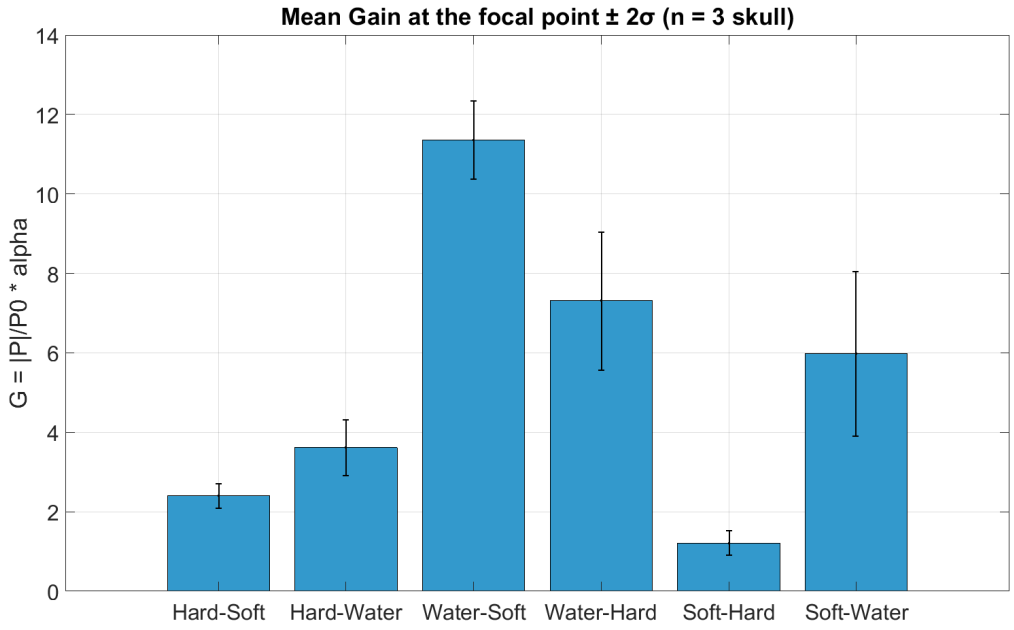


Figure 4.5: Mean acoustic gain ($G = |P|/|P_0| \cdot \alpha$) for each configuration, averaged across the three skull samples. Error bars represent the standard deviation ($\pm 2\sigma$), reflecting variability across skull anatomies.

Table 4.1: Mean acoustic gain G and associated uncertainty ($\pm 2\sigma$) across the three skull samples for each configuration.

Configuration	**Acoustic Gain** $G \pm 2\sigma$
Water–Soft	11.36 ± 0.99
Water–Hard	7.32 ± 1.74
Hard–Water	3.62 ± 0.70
Soft–Water	5.98 ± 2.08
Hard–Soft	2.40 ± 0.32
Soft–Hard	1.21 ± 0.31

Among all tested configurations, the *Water–Soft* case yields the highest gain (11.36 ± 0.99), demonstrating optimal energy coupling and focusing performance. The *Water–Hard* configuration also exhibits substantial gain (7.32 ± 1.74), albeit with a larger variability, suggesting that the introduction of a high-impedance layer introduces moderate distortion while preserving a significant portion of the focal energy. Intermediate performance is observed for the *Soft–Water* and *Hard–Water* configurations, with gains of 5.98 ± 2.08 and 3.62 ± 0.70, respectively. These results indicate partial loss of focusing efficiency due to asymmetrical impedance transitions, which affect wavefront coherence. In contrast, configurations involving both soft and hard media in transition—*Hard–Soft* and *Soft–Hard*—present the lowest gains, 2.40 ± 0.32 and 1.21 ± 0.31, respectively. These results clearly illustrate the detrimental effect of multiple impedance mismatches and skull-induced aberrations on acoustic energy deposition.

4.2.2 Focal deviation

The focal deviation computed from the simulation is presented in Figure 4.6. The corresponding numerical values for each configuration are provided in Table 4.2, allowing for a detailed assessment of the accuracy with which each lens configuration converges to the intended focus.

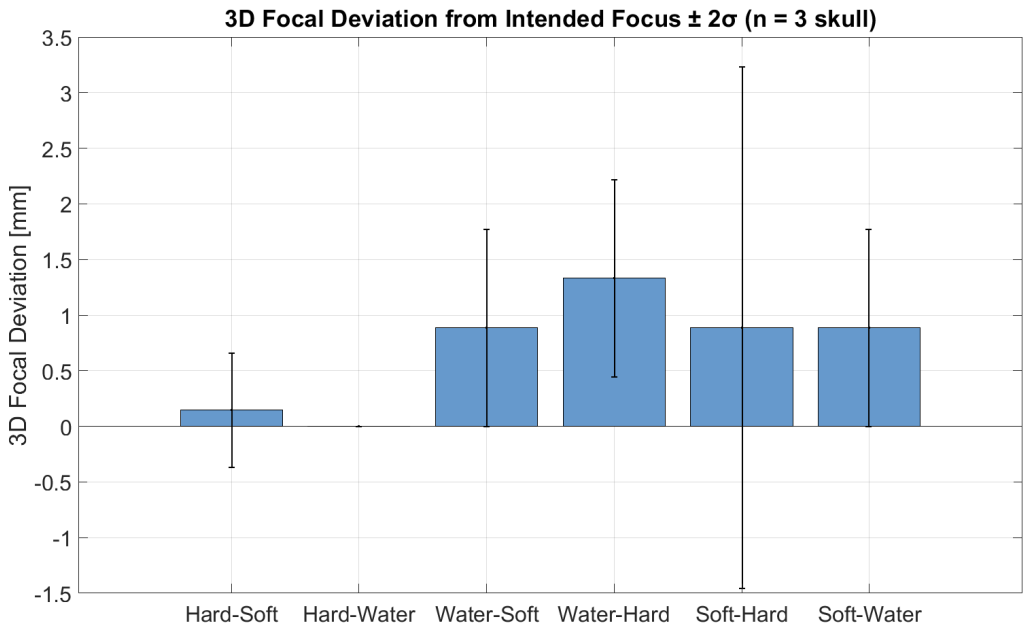


Figure 4.6: Mean focal devitation for each configuration, averaged across the three skull samples. Error bars represent the standard deviation ($\pm 2\sigma$), reflecting variability across skull anatomies.

Table 4.2: Mean devitation Δd and associated uncertainty ($\pm 2\sigma$) across the three skull samples for each configuration.

Configuration	**Deviation** $\Delta d \pm 2\sigma$ **[mm]**
Water–Soft	0.89 ± 0.89
Water–Hard	1.33 ± 0.89
Hard–Water	0.00 ± 0.00
Soft–Water	0.89 ± 0.89
Hard–Soft	0.15 ± 0.51
Soft–Hard	0.89 ± 2.35

The *Water–Hard* configuration shows the highest focal deviation (1.33 ± 0.89 mm), indicating that combining a soft coupling medium with a hard lens material may significantly reduce focal accuracy. In contrast, the *Hard–Water* configuration yields no measurable deviation (0.00 ± 0.00 mm), suggesting near-ideal focus preservation in this setup. Similarly, *Hard–Soft* (0.15 ± 0.51 mm) support the idea that rigid matching layers in contact with the skull better preserve the wavefront coherence. Both *Water–Soft* and *Soft–Water* present moderate deviations (0.89 ± 0.89 mm), which indicates relatively good but slightly more variable behavior. The *Soft–Hard* case exhibits a moderate mean deviation (0.89 mm) but the largest uncertainty (± 2.35 mm), reflecting high variability between skulls, specifically in x-axis. Overall, configurations involving rigid lens materials and low-impedance coupling media tend to offer more reliable and precise focusing.

4.2.3 Depth of focus

The depth of focus (DOF) computed from the simulation is presented in Figure 4.7. The corresponding numerical values for each configuration are provided in Table 4.3, offering

a comprehensive comparison of the lens's focal performance.

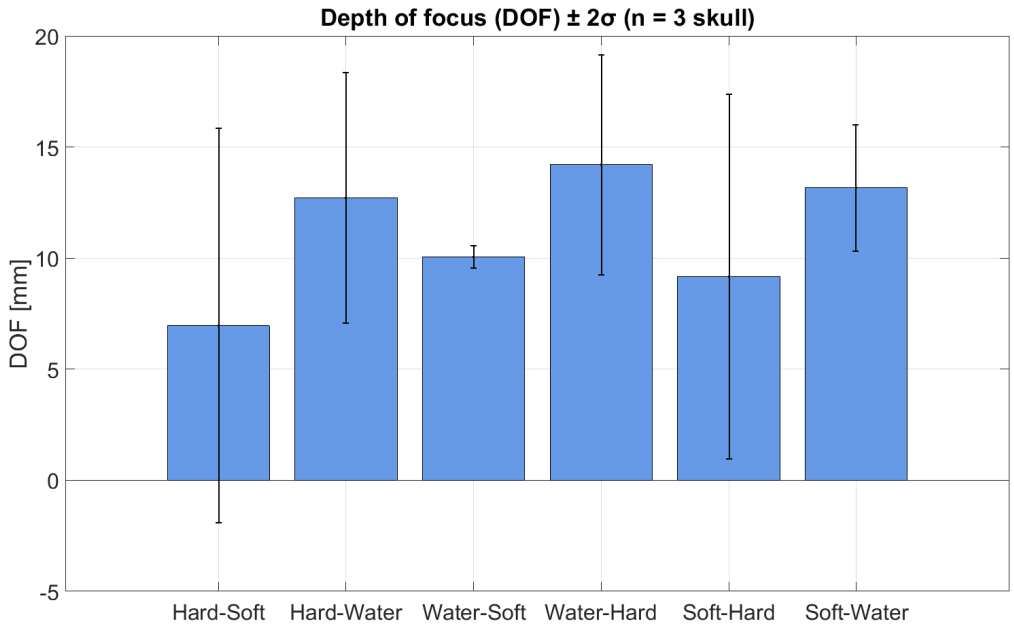


Figure 4.7: Mean depth of focus for each configuration, averaged across the three skull samples. Error bars represent the standard deviation ($\pm 2\sigma$), reflecting variability across skull anatomies.

Table 4.3: Mean depth of focus DOF and associated uncertainty ($\pm 2\sigma$) across the three skull samples for each configuration.

Configuration	**Depth of focus** $DOF \pm 2\sigma$ **[mm]**
Water–Soft	10.06 ± 0.51
Water–Hard	14.20 ± 4.94
Hard–Water	12.72 ± 5.63
Soft–Water	13.17 ± 2.85
Hard–Soft	6.95 ± 8.89
Soft–Hard	9.17 ± 8.20

The results show that the *Water–Hard* configuration achieves the highest mean depth of focus (DOF) with a value of 14.20 ± 4.94 mm, indicating excellent axial confinement of the acoustic beam. Similar performance is observed for the *Soft–Water* (13.17 ± 2.85 mm) and *Hard–Water* (12.72 ± 5.63 mm) combinations, followed closely by *Water–Soft* (10.06 ± 0.51 mm). These results suggest that configurations incorporating water as either the lens or coupling medium promote effective focusing along the propagation axis, likely due to better acoustic impedance matching and reduced scattering at material interfaces. On the other hand, the *Hard–Soft* and *Soft–Hard* combinations exhibit notably lower mean DOF values of 6.95 ± 8.89 mm and 9.17 ± 8.20 mm, respectively, along with high variability. These configurations involve transitions between materials with significantly mismatched acoustic properties. As a result, the focal beam becomes more diffuse or distorted, and the DOF measured above the 50% pressure threshold is substantially reduced.

4.2.4 Full Width at Half Maximum (FWHM)

The Full Width at Half Maximum (FWHM) computed from the simulation is presented in Figure 4.8. The corresponding numerical values for each configuration are listed in Table 4.4, enabling a comprehensive comparison of the lens's focal performance under different coupling conditions and offering deeper insight into the beam-shaping capabilities.

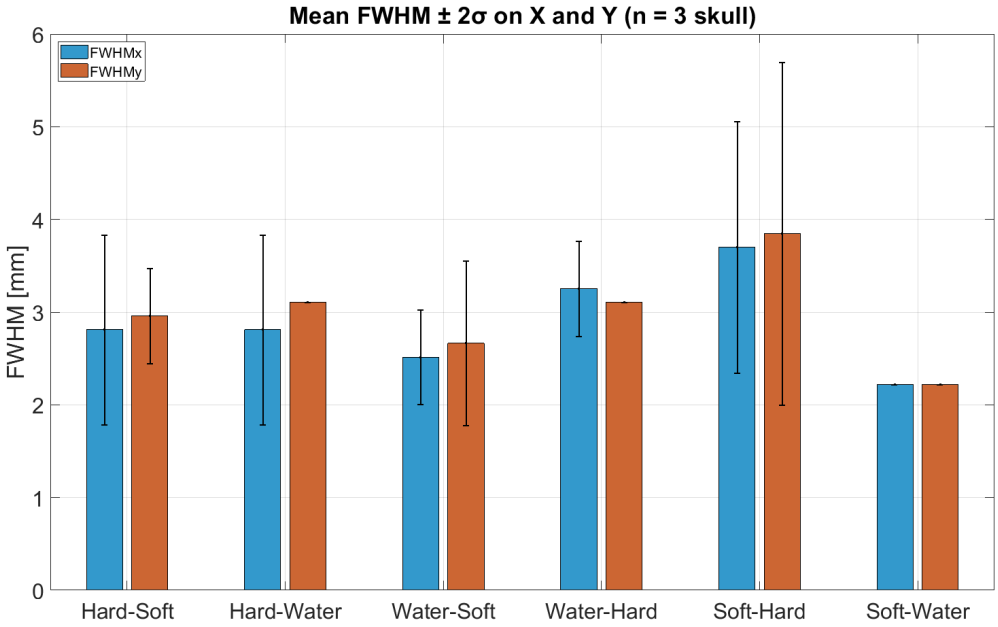


Figure 4.8: Mean FWHM for each configuration, averaged across the three skull samples. Error bars represent the standard deviation ($\pm 2\sigma$), reflecting variability across skull anatomies.

Table 4.4: Mean full width at half maximum (FWHM) in the X and Y directions across the three skull samples for each configuration. Uncertainty is expressed as $\pm 2\sigma$.

Configuration	$\mathbf{FWHM_X}$ **[mm]**	$\mathbf{FWHM_Y}$ **[mm]**
Water–Soft	2.51 ± 0.51	2.66 ± 0.89
Water–Hard	3.25 ± 0.51	3.11 ± 0.00
Hard–Water	2.81 ± 1.03	3.11 ± 0.00
Soft–Water	2.22 ± 0.00	2.22 ± 0.00
Hard–Soft	2.81 ± 1.03	2.96 ± 0.51
Soft–Hard	3.70 ± 1.37	3.85 ± 1.85

The *Water–Soft* configuration exhibits the most confined and symmetric focal spot,

with $\mathrm{FWHM_X} = 2.51 \pm 0.51$ mm and $\mathrm{FWHM_Y} = 2.66 \pm 0.89$ mm. This suggests high lateral resolution and effective energy focusing, aligning well with the pressure field distributions previously observed. The *Water–Hard* combination shows slightly broader lateral spreads (up to 3.25 mm), but with near-zero variability in the Y-direction, indicating consistent beam formation along this axis. Similarly, the *Hard–Water* and *Hard–Soft* cases maintain moderate confinement, though they present greater variability in beam width—likely due to the acoustic impedance mismatches that introduce aberrations and distort the focal region. In contrast, the *Soft–Hard* configuration produces the broadest and most variable lateral beam widths, with $\mathrm{FWHM_Y}$ reaching 3.85 ± 1.85 mm. This underscores the challenges of maintaining stable focusing across varying anatomies. Such discontinuities lead to phase distortions that degrade lateral resolution and introduce spatial inconsistencies in the focal region.

Chapter 5

Conclusions

This work presents the development of a holographic lens tailored for transcranial ultrasound therapies, with the aim of enhancing the acoustic coupling between the device and the patient's head. The approach accounts for the anatomical complexity of the skull and seeks to improve clinical feasibility by exploring coupling media beyond conventional water. Numerical simulations are employed to generate the lens design based on a specified focal point and to evaluate its performance across six material configurations, each combining a different pair of materials—one for the lens body and another for the coupling medium.

The results of the numerical simulations demonstrate that the choice of materials for the lens and coupling medium significantly influences the focusing performance of the holographic lens. To quantitatively evaluate the behaviour of the different material combinations used in the lens design, several key parameters were extracted from the results of the numerical simulations. These parameters include the acoustic gain, focal deviation, depth of focus and full width at half maximum (FWHM). Each of these metrics

is computed for every configuration and skull sample, providing detailed insight into the lens's focusing achievement and its ability to concentrate ultrasound energy at the focal spot. The results obtained from these metrics are associated with an uncertainty, which is estimated by conducting simulations on three different ex-vivo skull samples. This approach allows for the assessment of inter-subject variability.

The analysis of the acoustic gain reveals that configurations involving water as a coupling medium consistently outperform those using silicone or resin, achieving higher pressure amplitudes at the focal point, indicating optimal energy transfer and minimal distortion. In contrast, configurations with combinations of soft and hard materials exhibit lower gains due to increased impedance mismatches and wavefront aberrations.

The focal deviation results indicate that configurations combining hard lens materials with low-impedance coupling media achieve the most accurate alignment. The *Hard–Water* configuration, in particular, shows no measurable deviation, suggesting that the lens effectively compensates for skull-induced phase distortions. In contrast, configurations involving transitions between soft and hard materials demonstrate significant focal misalignment.

The depth of focus is particularly noteworthy, as it highlights the ability of the lens to maintain effective focusing over a range of depths. The *Water–Hard* configuration exhibits the greatest depth of focus, indicating that the pairing of water as a coupling medium with a hard lens material facilitates effective energy transmission through the skull. In contrast, configurations with soft materials as lens exhibit significantly reduced depth of focus, indicating that these combinations are less effective in maintaining a well-defined focal region.

Finally, the FWHM results indicate that the *Water–Soft* configuration achieves the tightest lateral confinement of the acoustic beam, while combinations involving hard mate-

rials exhibit broader beam widths, suggesting reduced lateral resolution. This is consistent with the observed pressure distributions, where water-based configurations demonstrate more localized and intense focal regions.

The findings of this study underscore the importance of material selection in the design of holographic lenses for transcranial ultrasound applications. The results suggest that using water as a coupling medium can significantly enhance the focusing performance of the lens, leading to improved therapeutic outcomes. Conversely, configurations involving hard/soft materials without a water medium, tend to introduce greater aberrations and reduce the overall effectiveness of the lens design.

5.1 Future work

Once the simulations are completed, the next step is to fabricate the holographic lens and conduct experimental validation of the numerical results. This involves manufacturing the lens using the selected materials and testing its performance in a controlled laboratory setting. The experimental setup will be designed to replicate the conditions of the numerical simulations, allowing for a direct comparison between simulated and measured acoustic fields. The experimental validation will include measuring the acoustic pressure distribution at the focal point, as well as evaluating the same metrics used in the numerical simulations, such as acoustic gain, focal deviation, depth of focus, and FWHM. This will provide a comprehensive assessment of the lens's performance and its ability to concentrate ultrasound energy at the target region.

Bibliography

[1] J. Kubanek, "Neuromodulation with transcranial focused ultrasound," *Neurosurgical Focus*, vol. 44, no. 2, 2018.

[2] R. Arulpragasam, M. Wout-Frank, J. Barredo, C. Faucher, B. Greenberg, and N. Philip, "Low intensity focused ultrasound for non-invasive and reversible deep brain neuromodulation – a paradigm shift in psychiatric research," *Frontiers in Psychiatry*, vol. 13, 2022.

[3] C. Horodyckid, M. Canney, A. Vignot, *et al.*, "Safe long-term repeated disruption of the blood-brain barrier using an implantable ultrasound device: A multiparametric study in a primate model," *Journal of Neurosurgery*, vol. 126, pp. 1–11, Jun. 2016.

[4] A. Carpentier *et al.*, "Clinical trial of blood-brain barrier disruption by pulsed ultrasound," *Science Translational Medicine*, vol. 8, no. 343, 343re2, 2016. DOI: 10.1126/scitranslmed.aaf6086.

[5] A. Pouliopoulos, S.-Y. Wu, M. Burgess, M. Karakatsani, H. Kamimura, and E. Konofagou, "A clinical system for non-invasive blood–brain barrier opening using a neuronavigation-guided single-element focused ultrasound transducer," *Ultrasound in Medicine and Biology*, vol. 46, Oct. 2019.

[6] O. Al-Bataineh, J. Jenne, and P. Huber, "Clinical and future applications of high intensity focused ultrasound in cancer," *Cancer Treatment Reviews*, vol. 38, no. 5, pp. 346–353, 2012.

[7] A. Abrahão, Y. Meng, M. Llinas, *et al.*, "First-in-human trial of blood–brain barrier opening in amyotrophic lateral sclerosis using mr-guided focused ultrasound," *Nature Communications*, vol. 10, Dec. 2019. DOI: 10.1038/s41467-019-13770-4.

[8] K. Hynynen, "Mri-guided focused ultrasound treatments," *Ultrasonics*, vol. 50, no. 2, pp. 221–229, 2010.

[9] K. Melde, A. G. Mark, T. Qiu, and P. Fischer, "Holograms for acoustics," *Nature*, vol. 537, pp. 518–522, 2016. DOI: 10.1038/nature19755.

[10] G. Maimbourg, A. Houdouin, T. Deffieux, M. Tanter, and J.-F. Aubry, "3d-printed adaptive acoustic lens as a disruptive technology for transcranial ultrasound therapy using single-element transducers," *Physics in Medicine and Biology*, vol. 63, p. 025 026, 2018.

[11] S. Jiménez-Gambín, N. Jiménez, J. M. Benlloch, and F. Camarena, "Holograms to focus arbitrary ultrasonic fields through the skull," *Phys. Rev. Applied*, vol. 12, p. 014 016, Jul. 2019.

[12] D. Gabor, "A new microscopic principle," *Nature*, vol. 161, pp. 777–778, 1948.

[13] G. Maimbourg, A. Houdouin, T. Deffieux, M. Tanter, and J.-F. Aubry, "3d-printed adaptive acoustic lens as a disruptive technology for transcranial ultrasound therapy using single-element transducers," *Physics in Medicine & Biology*, vol. 63, no. 2, p. 025 026, 2018. DOI: 10.1088/1361-6560/aaa037.

[14] N. McDannold *et al.*, "Non-invasive blood-brain barrier disruption using acoustic holography with a clinical focused ultrasound system," *IEEE Transactions on*

Biomedical Engineering, vol. 71, no. 10, pp. 3046–3054, Oct. 2024. DOI: 10.1109/TBME.2024.3407678.

[15] M. D. Brown, B. T. Cox, and B. E. Treeby, "Design of multi-frequency acoustic kinoforms," *Applied Physics Letters*, vol. 111, p. 244 101, 2017.

[16] Y. Hertzberg and G. Navon, "Bypassing absorbing objects in focused ultrasound using computer generated holographic technique," *Medical Physics*, vol. 38, pp. 6407–6415, 2011.

[17] G. T. Clement and K. Hynynen, "A non-invasive method for focusing ultrasound through the human skull," *Physics in Medicine and Biology*, vol. 47, no. 8, pp. 1219–1236, 2002.

[18] Y. Hertzberg and G. Navon, "Bypassing absorbing objects in focused ultrasound using computer generated holographic technique," *Medical Physics*, vol. 38, no. 12, pp. 6407–6415, 2011.

[19] P. Zhang, T. Li, J. Zhu, *et al.*, "Generation of acoustic self-bending and bottle beams by phase engineering," *Nature Communications*, vol. 5, p. 4316, 2014. DOI: 10.1038/ncomms5316.

[20] S. Jiménez-Gambín, N. Jiménez, and F. Camarena, "Transcranial focusing of ultrasonic vortices by acoustic holograms," *Physical Review Applied*, vol. 14, p. 054 070, 2020.

[21] D. Andrés, N. Jiménez, J. M. Benlloch, and F. Camarena, "Numerical study of acoustic holograms for deep-brain targeting through the temporal-bone window," *Ultrasound in Medicine and Biology*, 2024, To be published.

[22] N. Jiménez, J.-P. Groby, and V. Romero-García, "Spiral sound-diffusing metasurfaces based on holographic vortices," *Scientific Reports*, vol. 11, p. 10 217, 2021. DOI: 10.1038/s41598-021-89664-2.

[23] P. Gélat, G. T. Haar, and N. Saffari, "A comparison of methods for focusing the field of a hifu array transducer through human ribs," *Physics in Medicine and Biology*, vol. 59, pp. 3139–3154, 2014.

[24] K. Hynynen and F. A. Jolesz, "Demonstration of potential noninvasive ultrasound brain therapy through an intact skull," *Ultrasound in Medicine and Biology*, vol. 24, pp. 275–283, 1998.

[25] T. J. Dubinsky, C. Cuevas, M. K. Dighe, O. Kolokythas, and J. H. Hwang, "High-intensity focused ultrasound: Current potential and oncologic applications," *American Journal of Roentgenology*, vol. 190, no. 1, pp. 191–199, 2008. DOI: 10.2214/AJR.07.2671.

[26] T. L. Szabo, *Diagnostic Ultrasound Imaging: Inside Out*. Academic Press, 2004.

[27] G. ter Haar and C. Coussios, "High intensity focused ultrasound: Physical principles and devices," *International Journal of Hyperthermia*, vol. 23, pp. 89–104, 2007.

[28] D. Andrés, J. Vappou, N. Jiménez, *et al.*, "Thermal holographic patterns for ultrasound hyperthermia," *Applied Physics Letters*, vol. 120, no. 8, p. 084 102, 2022. DOI: 10.1063/5.0081565.

[29] A. Franzini, S. Moosa, D. Servello, *et al.*, "Ablative brain surgery: An overview," *International Journal of Hyperthermia*, vol. 36, no. 2, pp. 64–80, 2019. DOI: 10.1080/02656736.2019.1616833.

[30] Z. Xu, T. L. Hall, E. Vlaisavljevich, and F. T. Lee Jr, "Histotripsy: The first non-invasive, non-ionizing, non-thermal ablation technique based on ultrasound," *International Journal of Hyperthermia*, vol. 38, no. 1, pp. 561–575, 2021. DOI: 10.1080/02656736.2021.1905189.

[31] A. Randad, M. A. Ghanem, M. R. Bailey, and A. D. Maxwell, "Design, fabrication, and characterization of broad beam transducers for fragmenting large renal calculi with burst wave lithotripsy," *The Journal of the Acoustical Society of America*, vol. 148, pp. 44–50, 2020. DOI: 10.1121/10.0001475.

[32] S. Jiménez-Gambín, N. Jiménez, A. N. Pouliopoulos, J. M. Benlloch, E. E. Konofagou, and F. Camarena, "Acoustic holograms for bilateral blood-brain barrier opening in a mouse model," *IEEE Transactions on Biomedical Engineering*, vol. 69, no. 4, pp. 1359–1370, 2022. DOI: 10.1109/TBME.2021.3139799.

[33] J. Sun and K. Hynynen, "Focusing of therapeutic ultrasound through a human skull: A numerical study," *Journal of the Acoustical Society of America*, vol. 104, no. 3, pp. 1705–1715, 1998.

[34] C. R. Hill, J. Bamber, and G. T. Haar, *Physical Principles of Medical Ultrasonics*. New York, Chichester, Brisbane, Toronto: John Wiley & Sons, 2004.

[35] U. Schneider, E. Pedroni, and A. Lomax, "The calibration of ct hounsfield units for radiotherapy treatment planning," *Physics in Medicine and Biology*, vol. 41, pp. 111–124, Feb. 1996.

[36] T. D. Mast, "Empirical relationships between acoustic parameters in human soft tissues," *Acoustics Research Letters Online (ARLO)*, vol. 1, Nov. 2000.

[37] B. Treeby, B. Cox, and J. Jaros, *k-Wave: A MATLAB toolbox for the time domain simulation of acoustic wave fields. User Manual*, Manual Version 1.1 (August 27, 2016), Toolbox Release 1.1, 2016.

[38] J. Rodríguez-Sendra, A. Carrión, and F. Camarena, "Ultrasonic measurement of orthotropic elastic constants of 3d-printed photopolymer materials," in *2022 IEEE International Ultrasonics Symposium (IUS)*, cit. on p. 14, 2022, pp. 1–3. DOI: 10.1109/IUS54386.2022.9957208.

[39] B. E. Treeby, J. Jaros, A. P. Rendell, and B. T. Cox, "Modeling nonlinear ultrasound propagation in heterogeneous media with power law absorption using a k-space pseudospectral method," *The Journal of the Acoustical Society of America*, vol. 131, no. 6, pp. 4324–4336, 2012.

[40] IT'IS Foundation. "Tissue properties database: Acoustic properties – attenuation constant." Accessed: 2025-07-17. (2023), [Online]. Available: `https://itis.swiss/virtual-population/tissue-properties/database/acoustic-properties/attenuation-constant/`.

[41] N. Jiménez, V. Romero-García, V. Pagneux, and J.-P. Groby, "Quasiperfect absorption by subwavelength acoustic panels in transmission using accumulation of resonances due to slow sound," *Physical Review B*, vol. 95, p. 014 205, 2017.